A Phase Error Compensation Method for High-Rise Targets in High-Resolution SAR Images

JiaDong Deng, Wei Yang, Member, IEEE, HongCheng Zeng, Member, IEEE, YaMin Wang, Jiayi Guo, Wei Xiong, Min Liu, Jie Chen, Senior Member, IEEE, and Wei Liu, Senior Member, IEEE

Abstract—High-resolution images of urban areas generated by spaceborne synthetic aperture radar (SAR) have a wide range of applications. However, with the improvement in resolution, the slant range error caused by the height of buildings leads to high-order and complex phase errors during the imaging process, which in turn causes image defocusing. To address this issue, an optimization algorithm is proposed based on the conjugate gradient method to estimate and compensate for the phase error. It uses image entropy as the optimization objective function, which is applicable to segmented images, effectively solving the problem of variation of phase error at different heights. In addition, the algorithm improves the computational efficiency by introducing a restart strategy and a momentum term in the 1-D line search. Experimental results using both simulation and actual SAR data show that the proposed algorithm outperforms the existing methods in terms of both efficiency and focusing quality.

Index Terms—Conjugate gradient (CG) method, high-rise structure, image entropy, phase error estimation.

NOMENCLATURE

 θ Downward angle.

 φ Squint angle.

 v_r Equivalent velocity.

 φ_r Equivalent squint angle.

 f_d First-order Doppler parameter.

 f_r Second-order Doppler parameter.

 \mathbf{R}_s Satellite's position vector.

 \mathbf{V}_s Satellite's velocity vector.

 \mathbf{A}_s Satellite's acceleration vector.

 \mathbf{R}_t Target's position vector.

Received 24 April 2025; revised 22 June 2025; accepted 2 July 2025. Date of publication 14 July 2025; date of current version 30 July 2025. This work was supported by the National Key Research and Development Program of China under Grant 2022YFB3901601. (Corresponding authors: HongCheng Zeng; Min Liu.)

JiaDong Deng, Wei Yang, HongCheng Zeng, YaMin Wang, and Jie Chen are with the School of Electronic and Information Engineering, Beihang University, Beijing 100191, China (e-mail: djdong0725@buaa.edu.cn; yangweigigi@sina.com; zenghongcheng@buaa.edu.cn; wangyamin@buaa.edu.cn; chenjie@buaa.edu.cn).

Jiayi Guo is with the School of Information and Communication Engineering, Communication University of China, Beijing 100024, China (e-mail: jiayiguo@buaa.edu.cn).

Wei Xiong is with the Research Institute of information Fusion, PLA Naval Aviation University, Yantai 264001, China (e-mail: xiongwei@csif.org.cn).

Min Liu is with the Qian Xuesen Laboratory of Space Technology, China Academy of Space Technology (CAST), Beijing 100094, China (e-mail: ruiminlau@163.com).

Wei Liu is with the Department of Electrical and Electronic Engineering, The Hong Kong Polytechnic University, Kowloon Hong Kong (e-mail: wliu.eee@gmail.com).

Digital Object Identifier 10.1109/JSTARS.2025.3588656

- \mathbf{V}_t Target's velocity vector.
- \mathbf{A}_t Target's acceleration vector.
- $\{\Phi_k\}$ Phase errors.
- $\{\theta_k\}$ Compensation phase.
- $En(\cdot)$ Entropy function.
- $g(\cdot)$ Gradient function.
- d Search direction.
- p Directional derivative.

I. INTRODUCTION

PACEBORNE synthetic aperture radar (SAR) images have many applications in the fields of monitoring, interferometry, classification, and tomography [1], [2], [3], [4], [5]. With advancements in SAR imaging algorithms and systems in recent years, international high-resolution commercial SAR satellite systems have achieved a resolution of 0.3 m in the azimuth direction [6]. With high-resolution SAR images, the detection of high-rise structures and urban building changes as well as height measurements have become one of the most important parts in remote sensing applications [4], [5], [6], [7], [8], [9]. However, due to the influence of target height and errors from multipath effects, defocusing phenomenon may occur in high-rise areas, affecting accurate detection and interpretation of targets.

In order to obtain a well-focused target, automatic estimation of Doppler parameters is required to compensate for the residual phase errors. A few methods have been proposed for this purpose, such as the Map-drift algorithm (MD) and modified phase gradient autofocus (PGA) [10], [11]. The MD algorithm partitions the whole aperture data into two subapertures and calculates the Doppler parameter based on the cross-correlation results between these subapertures. A disadvantage of the MD algorithm is that it can only estimate two-order Doppler parameters, thereby falling short of fulfilling the demands posed by high-resolution SAR data imaging. Regarding the PGA algorithm, it can estimate the high-order Doppler parameters, but the performance will be significantly poor without isolated strong scatters in the image. Recent work addresses range-dependent phase errors in wide-swath SAR by subdividing ground range into narrow strips and employing overlapping subapertures, overcoming conventional PGA limitations and enhancing autofocus accuracy [12]. Recent deep learning-based SAR autofocus methods have been developed to compensate residual phase errors, with feasibility validated through image entropy evaluation in training and testing phases [13], [14]. By employing

a set of autofocus methods designed to optimize image metrics, the image quality can be improved with more complicated phase errors [15], [16], [17], [18], [19]. Applying different optimization algorithms, these autofocus methods based on image metrics determine the phase errors by maximizing or minimizing a particular image metric, such as image sharpness, contrast and entropy, on the defocused image intensity. Some of the optimization algorithms employed are gradient-descent techniques [16], quasi-Newton methods [17], [18], and adaptive momentum estimation (ADAM) methods [19]. The complexity of these solutions increases with the order of the phase error model, thus often necessitating a trade-off between optimization performance and processing efficiency. The conjugate gradient (CG) method is also a metric-based optimization technique that lies between the gradient descent (GD) method and the Newton's method [20]. Thanks to its conjugacy property, the CG method converges more rapidly than the GD method and avoids the need for computing the Hessian matrix and its inverse, which is a required step in Newton's method.

In high-resolution images, the tops of high-rise structures can become defocused. The slant range error caused by the height of these targets is a significant factor leading to image defocusing. The Doppler histories of targets at different heights are not identical, which means that the phase errors are space-variant in the range direction. However, the aforementioned methods do not take into account high-rise targets with this phase error variation.

In order to improve the focusing performance on tall building targets, in this article the phase errors caused by different height of the target are studied. An optimization algorithm based on CG is then proposed to determine phase errors on the single look complex (SLC) SAR images. To address the issue of space-variant phase errors, image entropy is employed as an objective function, which is particularly effective for segmenting the image into distinct blocks. And the gradient expression for the image entropy is also derived. Furthermore, this article incorporates a restart strategy and an interpolation line search technique including a momentum term, both of which are designed to enhance the efficacy of iterative optimization processes.

The rest of this article is organized as follows. Section II presents the SAR image formation problem for high-rise targets, and after analyzing the resultant phase errors, an SAR imaging model is constructed. The phase error estimation method based on CG is proposed in Section III. In Section IV, simulation data and actual SAR images are employed in numerical experiments to demonstrate the performance of the proposed method, including its computational complexity. Finally, Section V concludes this article.

II. PHASE ERROR AND SAR IMAGE MODEL

The low-frequency phase error introduced by building height is the main factor causing target defocusing. Therefore, this section analyses how target height generates phase errors and establishes a phase error model as well as a signal model of SAR images incorporating those errors.

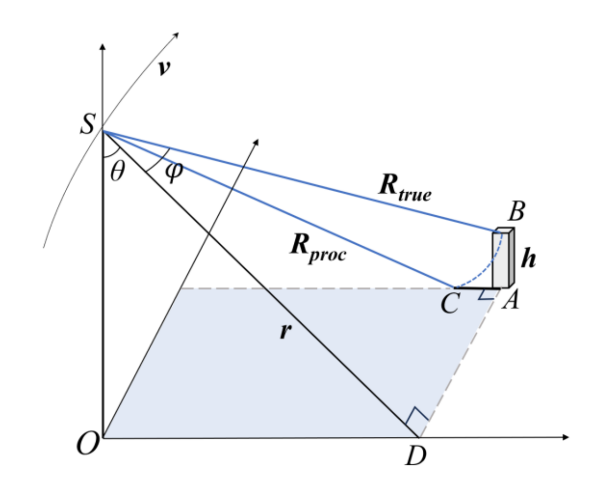


Fig. 1. Model for a high building target.

A. Phase Error of Target Height

As shown in Fig. 1, a satellite detects a building AB from point S. The satellite is at a height of H from the ground, while the height of the building is h. The point O is the subsatellite point and SD is the reference slant range of the scene, denoted as r. SOD forms a zero Doppler plane, with the downward angle represented as θ and the squint angle represented as φ .

From the model, the slant distance from the satellite to the building's top is denoted as $R_{\rm true}$ (SB, true slant range). All targets in real image processing are assumed to lie on the same slant-range plane. In this scenario, target B is imaged at the nearrange point C on the ground within the same azimuth time, where $R_{\rm true}$ either equals the satellite-to-ground distance $R_{\rm proc}$ (SC, processed slant range) or differs by less than one resolution cell. Consequently, after image formation processing, building AB is represented in the SAR image by the pixel units corresponding to AC.

In high-resolution spaceborne SAR imaging, the slant-range model must retain higher order terms due to nonnegligible satellite orbital curvature and prolonged synthetic aperture time. While this study does not focus on high-resolution SAR imaging and excludes residual errors beyond the classical squint-equivalent range model, the radical term (square-root expression) in the slant-range equation is expanded to sixth-order via Taylor series to analyze dominant phase errors induced by target height as follows:

$$R(t;r) \approx \sqrt{r^2 + (v_r t)^2 - 2rv_r t \sin \varphi_r}$$

$$\approx r - \frac{\lambda}{2} \frac{2v_r \sin \varphi_r}{\lambda} t + \frac{\lambda}{4} \frac{2v_r^2 \cos^2 \varphi_r}{\lambda r} t^2$$

$$+ \frac{\lambda}{2} \frac{v_r^3 \sin \varphi_r \cos^2 \varphi_r}{\lambda r^2} t^3$$

$$+ \frac{\lambda}{8} \frac{v_r^3 v_r \cos^2 \varphi_r (5\sin^2 \varphi_r - 1)}{\lambda r^3} t^4$$

$$+ \frac{\lambda}{8} \frac{v_r^5}{\lambda r^4} \left(-3 \sin \varphi_r + 10 \sin^3 \varphi_r - 7 \sin^5 \varphi_r \right) t^5$$

$$+\frac{\lambda}{16} \frac{v_r^6}{\lambda r^5} \left(1 - 15\sin^2\varphi_r + 35\sin^4\varphi_r - 21\sin^6\varphi_r\right) t^6 \tag{1}$$

where both v_r and φ_r can be derived from the first-order Doppler parameter f_d and the second-order Doppler parameter f_r , as expressed in the following equations:

$$\begin{cases} v_r = \sqrt{\left(\frac{\lambda f_d}{2}\right)^2 - \frac{\lambda r f_r}{2}} \\ \varphi_r = \arcsin\left(\frac{\lambda f_d}{2v_r}\right) \end{cases}$$
 (2)

$$f_d = -\frac{2}{\lambda} \frac{(\mathbf{R}_s - \mathbf{R}_t) (\mathbf{V}_s - \mathbf{V}_t)}{r}$$
(3)

$$f_r = -\frac{1}{\lambda} \frac{4(\mathbf{V}_s - \mathbf{V}_t)^2 + 4(\mathbf{R}_s - \mathbf{R}_t)(\boldsymbol{\alpha}_s - \mathbf{A}_t) - \lambda^2 f_d^2}{2r}$$
(4)

where \mathbf{R}_s , \mathbf{V}_s , and \mathbf{A}_s denote the satellite's position vector, velocity vector, and acceleration vector at the azimuth zero time (the instant when the beam center illuminates the target), while \mathbf{R}_t , \mathbf{V}_t , and \mathbf{A}_t represent the target's corresponding vectors at the same reference time, respectively. For real target B and imaged target C, they share identical satellite parameters \mathbf{R}_s , \mathbf{V}_s , and \mathbf{A}_s at the same azimuth time. Their distinction lies in their respective position, velocity, and acceleration vectors within the Earth-centered, Earth-fixed (ECEF) coordinate system. Assume that target B has coordinates (x,y) in the slant-range plane, where x and y correspond to the azimuth and range directions, respectively. The scene center's geodetic coordinates are (Λ_0, Ψ_0) , with Λ_0 and Ψ_0 denoting longitude and latitude. The target's geodetic coordinates (Λ_t, Ψ_t) and the geocentric distance to its ground projection R_e can be calculated as follows:

$$\Lambda_{t} = \Lambda_{0} + y \cdot \frac{\|E_{a} \sin \Psi_{0}, E_{b} \cos \Psi_{0}\|_{2}}{E_{a} E_{b} \sin \Psi_{0}}
\Psi_{t} = \Psi_{0} + x \cdot \frac{\|E_{a} \sin \Psi_{0}, E_{b} \cos \Psi_{0}\|_{2}}{E_{c} E_{t}}$$
(5)

$$R_E = \frac{E_a E_b}{\|E_a \sin(\Psi_t), E_b \cos(\Psi_t)\|_2}$$
 (6)

where E_a and E_b represent the Earth's semimajor axis and semiminor axis, respectively. Accounting for the target's height h, its geocentric position vector in the Earth-centered inertial coordinate system can be expressed as follows:

$$\mathbf{R}_{o} = \begin{bmatrix} x_{o} \\ y_{o} \\ y_{o} \end{bmatrix} = (R_{E} + h) \begin{bmatrix} \cos \Psi_{t} \cos \Lambda_{t} \\ \cos \Psi_{t} \sin \Lambda_{t} \\ \sin \Psi_{t} \end{bmatrix}. \tag{7}$$

And in the ECEF coordinate system, the target's position, velocity, and acceleration vectors can be obtained as follows:

$$\mathbf{R}_{t} = \begin{bmatrix} x_{t} \\ y_{t} \\ y_{t} \end{bmatrix} = \begin{bmatrix} x_{o} \\ y_{o} \\ y_{o} \end{bmatrix} \begin{bmatrix} \cos\frac{x}{v_{\text{sw}}} \omega_{E} & \sin\frac{x}{v_{\text{sw}}} \omega_{E} & 0 \\ -\sin\frac{x}{v_{\text{sw}}} \omega_{E} & \cos\frac{x}{v_{\text{sw}}} \omega_{E} & 0 \\ 0 & 0 & 1 \end{bmatrix}$$
(8)

$$\mathbf{V}_{t} = \begin{bmatrix} v_{x} \\ v_{y} \\ v_{z} \end{bmatrix} = \begin{bmatrix} -y_{t} \\ x_{t} \\ 0 \end{bmatrix} \omega_{E} \tag{9}$$

TABLE I PARAMETERS FOR RANGE MODEL SIMULATION

Parameters	Values
Downward angle (deg)	15.0-60.0
Semimajor axis (m)	7003819.0
Eccentricity	0.0011
RAAN (deg)	0.0
Inclination (deg)	97.89
Argument of perigee (deg)	90.0
Synthetic aperture time (s)	12
Wavelength (m)	0.03125
Longitude and latitude of sub satellite point (deg)	(0.0,0.0)

$$\mathbf{A}_{t} = \begin{bmatrix} a_{x} \\ a_{y} \\ a_{z} \end{bmatrix} = \begin{bmatrix} -x_{t} \\ -y_{t} \\ 0 \end{bmatrix} \omega_{E}^{2} \tag{10}$$

where ω_E denotes Earth's angular velocity of rotation and $v_{\rm sw}$ denotes the imaging swath's velocity on the ground. For the imaged target point C, its coordinates in the slant-range plane can be $(x, y+\Delta y)$, with the target height h set to zero in (7). When slant ranges for targets B and C are equal, the corresponding height h and offset Δy are determined. Analysis reveals that although B and C share identical slant ranges, their components along each coordinate axis differ, as do their velocity and acceleration vectors. Consequently, they exhibit distinct range cell migration curves and Doppler parameters. Furthermore, compared to target B, target C accumulates phase errors during the synthetic aperture time due to these kinematic discrepancies. The two-way residual phase errors between two range models can be calculated using the following expression:

$$\varphi_{\text{error}}\left(t\right) = \frac{4\pi \left(R_{\text{true}}\left(t\right) - R_{\text{proc}}\left(t\right)\right)}{\lambda}.$$
 (11)

The following simulation analysis compares the phase errors induced by target height under different orders of Doppler parameters, with the orbital and radar parameters listed in Table I. With a 12 s synthetic aperture time, azimuth resolution of 0.1-m level can be achieved in imaging. And Fig. 2 illustrates the simulated two-way residual phases introduced at varying heights according (1) and (11).

The figure demonstrates that the quadratic phase error (QPE) dominates the phase errors, increasing by $\pi/3$ per 100-m altitude for downward angle 15°. The cubic phase term becomes secondary, reaching $\pi/20$ at 500 m. Higher order terms (quartic: ~ 0.05 rad, quintic: $\sim 10^{-6}$ rad) are negligible. The conclusion applies to single-point targets. Furthermore, the extent of deviation from true range migration for elevated targets is primarily governed by the downward angle. Fig. 2(a)–(d) simulates cases from 15° to 60°, respectively, and the results validate this observation. Under a 60° downward angle, the QPE introduced per 100-m altitude reduces to $\pi/8$.

And for high-rise structures composed of multiple strong point targets, a scenario was configured with a building measuring 100 m (length) \times 200 m (width) \times 450 m (height), where point targets are distributed with 10 m spacing in both lateral and longitudinal dimensions, and 15 m vertical spacing. The building

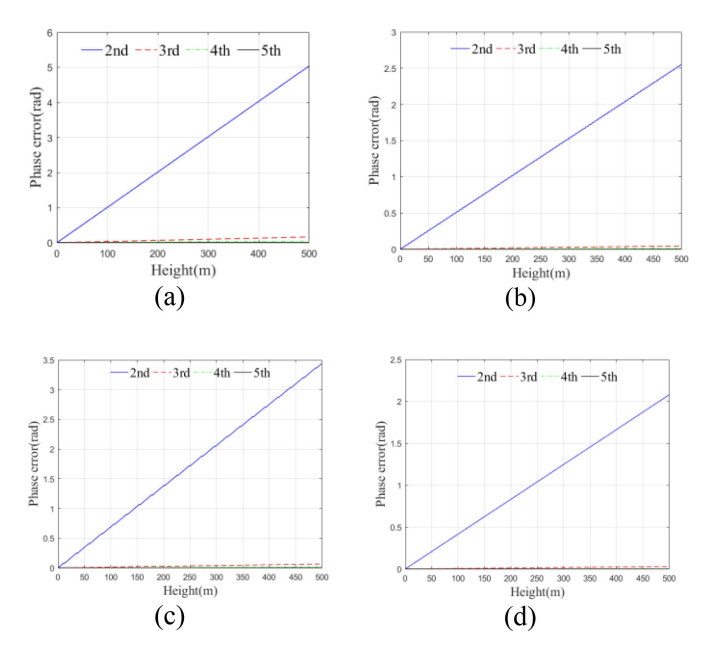


Fig. 2. Simulation for elevated targets. (a) Downward angle 15°. (b) Downward angle 30°. (c) Downward angle 45°. (d) Downward angle 60°.

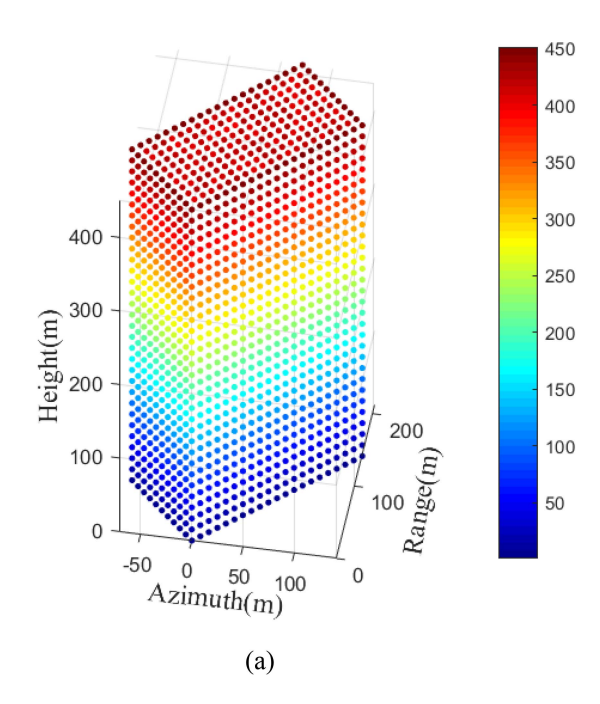
TABLE II
AZIMUTH METRICS FOR POINT TARGETS

Target height/m	0	50	100	200
IRW/m	0.260	0.263	0.271	0.343
PSLR/dB	-13.136	-12.428	-10.140	-4.285
ISLR/dB	-10.121	-9.396	-7.624	-6.077

is oriented at 45° relative to the azimuth direction, as illustrated in Fig. 3(a). Spaceborne SAR echo simulation and imaging are performed for this configuration and the final imaging result is shown in Fig. 3(b). The orbital parameters for simulation imaging adopted the values in Table I, with the resolution set to 0.5 m, referencing the parameters of the in-orbit satellite UMBRA-01.

Results indicate that the building's elevation is projected along the range direction in the image. The target base is well-focused, while significant defocusing is observed at the top. At the same azimuth time, multiple scatterers with approximately 50-m elevation differences coexist, as demonstrated by the target spanning three elevation sampling units at azimuth time t_a in the Fig. 3(b).

Azimuth profile analysis of point targets in Fig. 4 reveals that the 50-m elevation difference has a significant impact on imaging quality. The azimuth profile of the target at 0-m altitude shown in Fig. 4 is ideal. At 50-m altitude, there is noticeable elevation of the trough between the main lobe and sidelobe of the target. At 100-m altitude, elevation occurs in the target's sidelobe, while the target at 200-m altitude appears completely defocused in the azimuth direction.



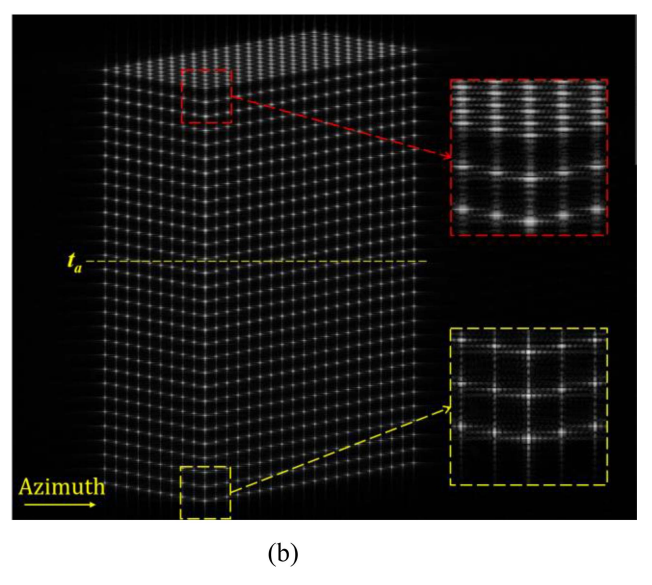


Fig. 3. Simulation for a high building target. (a) Simulation scenario. (b) Imaging result.

Quantitative azimuth metrics are detailed in Table II, which confirmed the above-mentioned analysis. Consequently, although phase errors primarily dominated by QPE, their spatially variant characteristics prevent effective global phase compensation through chirp rate estimation.

B. Phase Error Model

In SAR imaging phase errors can be categorized into low-frequency phase errors and high-frequency phase errors. Among them, low-frequency phase errors include linear (first-order) phase errors, second-order phase errors, and other higher order phase errors. High-frequency phase errors include high-frequency sinusoidal phase errors and broadband phase errors.

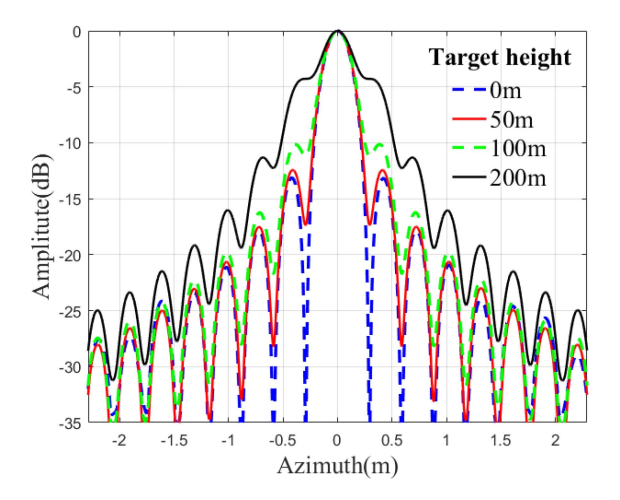


Fig. 4. Azimuth curves for targets.

For low-frequency errors, the first-order phase error solely results in shifting the whole image without impacting the focusing effect. Odd-order phase errors of third and above can cause the main lobe to widen and exhibit significant asymmetry, while even-order phase errors of higher orders can similarly widen the main lobe and increase the strength of the side lobes [19]. In range-Doppler frequency domain, the $p_{\rm th}$ order phase error model of the echo can be assumed as follows:

$$\Phi_k = \sum_{i=2}^p \mu_i \cdot k^i + \nu n_k \tag{12}$$

where Φ_k is the phase error in the k_{th} azimuth frequency point and μ_i is the i_{th} phase error coefficient. The second term denotes the random phase error to describe high-frequency phase errors, where ν is the coefficient and $n_1, ..., n_k$ are independent and identically distributed (i.i.d.) random variables following uniform distribution U(0,1).

However, in the real environments, varying scattering characteristics of building materials can lead to high-frequency phase errors, while multipath effects can result in wideband phase errors, which may simultaneously include complex low and high-frequency errors.

For example, Fig. 5 shows the surrounding area of Keangnam Landmark Tower 72 in Hanoi, Vietnam, captured under the spotlight mode of the UMBRA-01 satellite, with a resolution of 0.5 m.

The image is generally well-focused while there are locally defocused areas, particularly at the top of the buildings. The phase error of the entire image is estimated by the proposed method, and the error curve contains high-order errors and random errors, as shown in Fig. 6.

In summary, using Taylor expansion and random errors of (12) to describe the phase error in high-rise targets proves insufficient in terms of accuracy. To address this challenge, this study returns to the fundamental approach by directly treating various errors as a total phase error of the final synthesized azimuth spectrum, with precision down to each individual frequency point. The

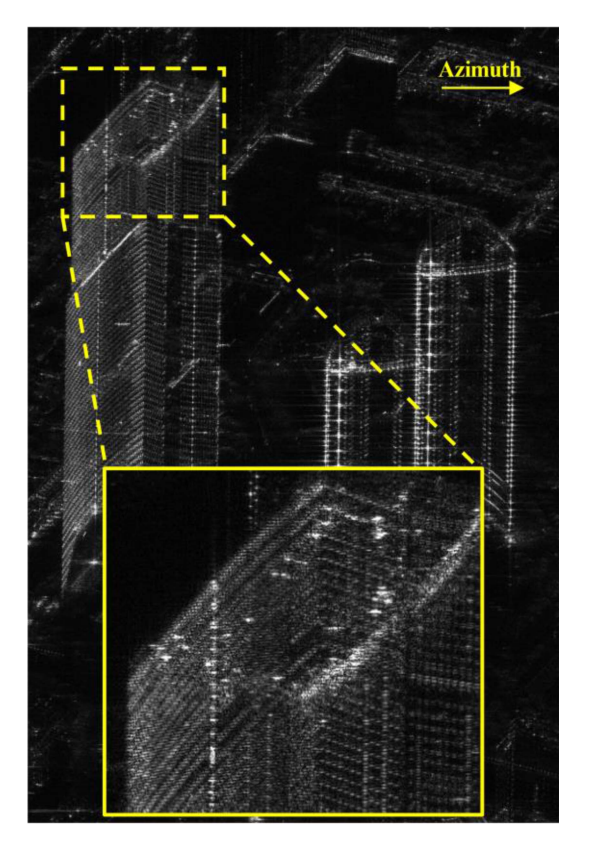


Fig. 5. Surrounding area of Keangnam Landmark Tower 72, Hanoi, Vietnam.

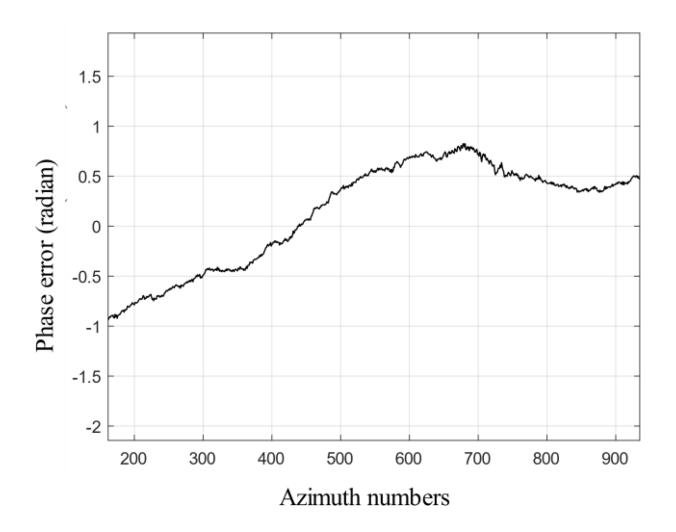


Fig. 6. Phase errors of Keangnam Landmark Tower 72.

specific representation is as follows:

$$F(k,n) = \tilde{F}(k,n) e^{j\Phi_k} \tag{13}$$

where F(k,n) represents the measured signal spectrum in the range-Doppler frequency domain after range compression and range migration correction, n denotes the range position, k denotes the azimuth frequency point, and $\tilde{F}(k,n)$ represents the corresponding signal spectrum without phase error. The problem is now transformed into determining the value of $\{\Phi_k\}$. Without

focusing on the phase error coefficients of each order, the model is capable of estimating both high-order and high-frequency phase errors.

C. SAR Image Model

Suppose that f(m, n) represents the measured SLC image value after image processing, where N is the number of sample points in range and M is the number of sample points in azimuth. Here, m is an index to the azimuth position. To estimate phase errors, f(m, n) can be given using the inverse fast Fourier transform (IFFT)

$$f(m,n) = \frac{1}{M} \sum_{k=0}^{M-1} F(k,n) \cdot e^{j\frac{2\pi}{M}mk}$$
$$= \frac{1}{M} \sum_{k=0}^{M-1} \tilde{F}(k,n) \cdot e^{j\Phi_k + j\frac{2\pi}{M}mk}. \tag{14}$$

By introducing a compensation phase $\{\theta_k\}$, the resulting compensated SLC image $f_{\text{comp}}(m,n)$ can be expressed as follows:

$$f_{\text{comp}}(m, n) = f(m, n) \otimes \exp\{j\theta_k\}. \tag{15}$$

To make f_{comp} the same as the desired complex image $f = \mathscr{F}\{F\}$, where $\mathscr{F}\{\cdot\}$ denotes fast Fourier transform (FFT), it can be concluded that $\{\theta_k\} = -\{\Phi_k\}$, thus achieving phase error compensation. By minimizing or maximizing an objective function $\psi(\centerdot)$ related to the complex image value $f_{\text{comp}}(m,n)$, the estimated compensation phase can be formulated as follows:

$$\theta_k = \underset{\theta_k}{\operatorname{arg\,max}} \psi(\theta_k) \operatorname{or\,arg\,min} \psi(\theta_k) k = 1, 2 \cdots M.$$
 (16)

In this way, a model only based on the measured complex image signal and the phase errors is established without relying on the internal calibration data or ephemeris parameters, or building a complex slant distance model. The specific form of the objective function and the estimation method are discussed in the following section.

III. PHASE ERROR COMPENSATION METHOD

Inferences about the phase errors must usually be made from the measured signal, which is a complicated mixture of both the unknown scene characteristics and the unknown phase errors. Thus, there is theoretically no analytical solution for (16). To address this joint inference problem, optimization is a popular approach [15], [16], [17], [18], [19], [22], [23]. In this way the phase error estimation problem is transformed into a multidimensional unconstrained optimization problem and our target is to find out the accurate value of $\{\theta_k\}$, by maximizing or minimizing an appropriate objective function, which is usually the image entropy, contrast or sharpness.

The minimum entropy criterion is firstly adopted as the objective function, which is formulated in terms of $\{\theta_k\}$. The CG algorithm is then employed to determine the search direction d_i for updating $\{\theta_k\}$ during the next iteration. At each iteration stage, a stepping method combined with interpolation method

is applied to perform 1-D line search along the determined direction d_i , thereby updating $\{\theta_k\}$ to minimize the current objective function value.

A. Minimum Entropy Criterion

Image entropy, image sharpness and image contrast can all describe the focusing effect of SAR images. When error compensation is completed, the image will be accurately focused, and the image entropy reaches its minimum value while the image sharpness and contrast reach their maximum value. Image entropy is approximately additive when dividing an image into smaller blocks, which allows for more efficient and accurate optimization in the proposed method. There are many definitions for image entropy [24], [25], [26], and we use the definition from [25] as the objective function in (17), while image sharpness and contrast serve as evaluation criteria for assessing image focusing quality in Section IV. The image entropy is defined as follows:

$$En = -\sum_{m,n}^{M \times N} \rho(m,n) \ln \rho(m,n)$$
 (17)

where $\rho(m,n)$ indicates the ratio of pixel energy to the total energy of the image. It is also called the pixel energy ratio and can be expressed as follows:

$$\rho(m,n) = \frac{|f(m,n)|^2}{C} = \frac{|f(m,n)|^2}{\sum_{i=0}^{M-1} \sum_{j=0}^{N-1} |f(i,j)|^2}$$
(18)

where C is the total energy of the image. As phase compensation only alters the phase of each pixel without changing its amplitude, the total energy of the image remains unchanged, i.e., C is a constant. In addition, since $\sum_{m,n}^{M\times N} \rho_{m,n} = 1$, the energy ratio for each pixel is significantly smaller than 1 in large-scale images. Consequently, we simplify (18) into the following form:

$$En = -\sum_{m,n}^{M \times N} \frac{|f(m,n)|^2}{C} \ln \frac{|f(m,n)|^2}{C} -\frac{1}{C} \sum_{m,n}^{M \times N} |f(m,n)|^2 \ln |f(m,n)|^2 + \ln C.$$
(19)

Now, divide the image into L subimages in the range direction. According to (19), the subentropy can be expressed as follows:

$$En_{l} = -\frac{1}{C_{l}} \sum_{m,n}^{M \times N_{l}} |f(m,n)|^{2} \ln |f(m,n)|^{2} + \ln C_{l}$$
 (20)

with $N = L \cdot N_l$ and $C = \sum_{l=1}^{L} C_l$, the image entropy and the subimage entropies are related by

$$\sum_{l}^{L} \frac{C_{l}}{C} E n_{l} = \sum_{l}^{L} \left(\frac{1}{C} \sum_{m,n}^{M \times N_{l}} \left| f(m,n) \right|^{2} \ln \left| f(m,n) \right|^{2} + \frac{C_{l}}{C} \ln C_{l} \right)$$

$$= En - \ln C + \sum_{l}^{L} \frac{C_l}{C} \ln C_l. \tag{21}$$

According to (20), image entropy can be expressed as a linear combination of subentropies. C_l/C represents the coefficient associated with each subentropy, while the second term and the third term denote a constant term. This linear property implies that the image reaches its optimal focusing effect when all subimages obtain the minimum entropy after phase compensation, resulting in the lowest possible entropy value for the entire image.

The separability of the objective function mentioned previously can enhance the accuracy and efficiency of the optimization algorithm. Due to the inconsistency of phase errors at different heights, the blockwise estimation of phase errors effectively contributes to improving the focus quality of the whole image. And the dependence between iterations makes it difficult to perform parallel acceleration. However, dividing the image into manageable sections allows for more efficient parallel processing.

B. 1-D Line Search

In optimization algorithms, after determining the initial direction of iteration and updating the iteration direction at each step, it is generally necessary to perform 1-D line search to determine the current compensation phase. In essence, through 1-D line search, we find the phase error value that minimizes the image entropy in the current direction.

The line search method employed here consists of two steps. The stepping method is employed to locate the interval where a minimum exists, followed by interpolation to determine the new compensation phase. This method is an effective approximate search technique. Due to introduction of the momentum term in the stepping method, it only requires a very small number of iterations to determine the extremum interval. Furthermore, the compensation phase is directly determined using quadratic interpolation, without the need for additional iterative operations.

The stepping method explores the monotonicity of the function by gradually increasing or decreasing the step size, thus identifying an interval that contains a minimum. It is crucial to initialize the step size appropriately. If it is too large, it may be challenging to define the search interval or locate it at all, and if it is too small, it can lead to inefficient iterations. To enhance efficiency, a momentum-based method is introduced to optimize the selection of the initial step

$$\begin{cases} h_{i+1} = \gamma s_i + (1 - \gamma) h_i \\ s_{i+1} = (is_i + h_{i+1})/i \end{cases}$$
 (22)

where h_i and s_i indicate the initial step and its mean value in the i_{th} iteration of the whole iteration process, and γ is the learning rate whose value is between 0 and 1.

A pseudocode representation of this part of the algorithm is shown in Table III.

After determining the interval, the interpolation method is used to determine the new compensate phase. We approximate the objective function by a quadratic function within this interval, and the coefficients of the quadratic function can be determined by the two endpoints and their first derivatives, thereby obtaining the phase of the minimum value.

To avoid the appearance of quadratic terms in interpolation calculation, the gradient needs to be calculated. For this purpose, we first obtain the following partial derivative:

$$\frac{\partial \left| f\left(m,n\right)\right|^{2}}{\partial \theta} = \frac{2}{M} \operatorname{Im} \left[f\left(m,n\right) \cdot F^{*}\left(k,n\right) \\ \cdot \exp\left(-j\theta_{k} - j\frac{2\pi}{N}mk\right) \right]$$
(23)

where ${\rm Im}\{\cdot\}$ denotes the imaginary component of complex values. Therefore, the gradient $g(\theta)$ of image entropy $En(\theta)$

TABLE III PSEUDOCODE FOR THE STEPPING METHOD

Algorithm1 Stepping method based on the momentum.

Input: Current compensate phase θ_i , current search direction p_i and current initial direction vector h_i .

Output: Search interval $[\theta_{\min}, \theta_{\max}]$ and new initial direction vector h_{i+1} .

1: Initialize the variables $x_1 = \theta_i$; $h = h_i$; $\gamma = 0.9$;

2: repeat

3: Compute the new direction vector $p = h_0 \cdot p_i$ and update the new phase $x_2 = x_1 + p$;

4: **if** (the entropy of the new phase is getting smaller) **then**

5: Advance the search interval forward $x_3 = x_1$; $x_1 = x_2$ and increase the size of the step h_0 .

6: **else if** (this is the first iteration) **then**

7: Change the sign of h_0 ;

8: end if

9: **until** (this is not the first iteration and the entropy of the new phase is bigger)

10: if (the step is positive) then

11: $\theta_{\min} = x_1; \theta_{\max} = x_2;$

12: else

13: $\theta_{\min} = x_2; \theta_{\max} = x_1;$

14: **end if**

15: Update the new initial direction vector h_{i+1} . // (22)

is given as follows:

ance mize
$$g(\theta) = \frac{\partial En(\theta)}{\partial \theta}$$

$$(22) = \frac{-1}{C} \sum_{m,n}^{M \times N} \left[\left(\frac{\partial |f|^2}{\partial |f|^2} \ln |f|^2 + |f|^2 \frac{\partial \ln |f|^2}{\partial |f|^2} + \frac{\partial \ln C}{\partial |f|^2} \right) \frac{\partial |f|^2}{\partial \theta} \right]$$
Value sithe
$$= \frac{-1}{C} \sum_{m=0}^{M-1} \sum_{n=0}^{N-1} \left\{ \left(\ln |f|^2 + 1 + 0 \right) \atop \frac{2}{M} \operatorname{Im} \left[f \cdot F^*(k,n) \exp(-j\theta_k - j\frac{2\pi}{N}nk) \right] \right\}$$
am is
$$= \frac{-2}{CM} \sum_{m=0}^{M-1} \operatorname{Im} \left\{ \sum_{n=0}^{F^*(m,k) \exp(-j\theta_k)} \left[\left(\ln |f(m,n)|^2 + 1 \right) \atop f(m,n) \exp(-j\frac{2\pi}{N}nk) \right] \right\}$$
and is mate in the sine
$$= -\frac{2}{CM} \sum_{m=0}^{M-1} \operatorname{Im} \left[F^*(m,k) \exp(-j\theta_k) T(m,k) \right]$$

$$= -\frac{2}{CM} \sum_{m=0}^{M-1} \operatorname{Im} \left[F^*(m,k) \exp(-j\theta_k) T(m,k) \right]$$

$$= -\frac{2}{CM} \sum_{m=0}^{M-1} \operatorname{Im} \left[F^*(m,k) \exp(-j\theta_k) T(m,k) \right]$$

$$= -\frac{2}{CM} \sum_{m=0}^{M-1} \operatorname{Im} \left[F^*(m,k) \exp(-j\theta_k) T(m,k) \right]$$

$$= -\frac{2}{CM} \sum_{m=0}^{M-1} \operatorname{Im} \left[F^*(m,k) \exp(-j\theta_k) T(m,k) \right]$$

where $T(m,k)=F\{f(m,n)(2\ln|f(m,n)|+1)\}$. It is important to note that in (24), partial derivatives $\partial En(\theta)/\partial \theta(k_1)$ and $\partial En(\theta)/\partial \theta(k_2)(k_1\neq k_2)$ are independent. This independence implies that each $\partial En(\theta)/\partial \theta(k_i)$ does not contain any other $\theta(k_j)(i\neq j)$ within its expression. And each θ_k converges rapidly towards its final value after each iteration. Consequently, the iteration is achievable and its convergence is fast, despite the presence of N variables that need to be estimated.

With the phase gradient expression, the new compensate phase can be calculated by

$$\begin{cases}
a = \frac{\theta_{\text{max}} - \theta_{\text{min}}}{2(g(\theta_{\text{max}}) \cdot d_i - g(\theta_{\text{min}}) \cdot d_i)} \\
b = g(\theta_{\text{min}}) \cdot d_i - 2a \cdot \theta_{\text{min}} \\
\theta_{i+1} = -\frac{b}{2a}
\end{cases}$$
(25)

where a and b represent the coefficients corresponding to the quadratic term and the linear term, respectively.

C. CG Method

The Fletcher–Reeves (FR) method adopted in this article is a CG method specifically designed for solving unconstrained optimization problems [27]. In each iteration, the FR method adjusts the search direction by utilizing the current search direction and gradient information, thereby gradually approaching the optimal solution. Its advantage lies in the conjugacy between directions d_i and d_{i+1} in consecutive iterations, which makes the method perform well in terms of convergence and computational efficiency. When dealing with nonquadratic problems, the FR method is similar to the BFGS quasi-Newton method, but it does not require the computation of an approximation of the Hessian matrix. Instead, it requires only the gradient of the objective function and calculates the search direction for the next iteration as follows:

$$d_{i+1} = \begin{cases} -g_i & i \mod Q = 0\\ -g_i + \frac{g_i^t \cdot g_i}{g_{i-1}^t \cdot g_{i-1}} \cdot d_i & \text{otherwise.} \end{cases}$$
 (26)

In (26), a restart strategy is employed in our method. With successive iterations, due to cumulative error arising from non-quadratic objective functions, convergence of the newly generated conjugate directions can become slow and the algorithm may even get stuck in a local minimum. To mitigate this issue, one effective method is to set $d_i = g$ and restart the iteration from the steepest descent direction every Q iteration.

Fig. 7 illustrates the flowchart of the proposed algorithm and Table IV presents its pseudocode.

The subsequent description outlines the steps of the algorithm as follows.

Step 1: Divide the image into L subimages.

Step 2: Perform the azimuth FFT operation on each subimage and initialize the compensation phase θ_0 , the search directional vector d_0 and the line search step h_0 and its mean value s_0 .

Step 3: Calculate the directional derivative p of the gradient g_i and its directional vector d_i

$$p = -d_i \cdot g_i. \tag{27}$$

Step 4: Employ line search proposed in the previous section to find a new compensation phase θ_{i+1} and update the line search step h_{i+1} .

Step 5: If the variation in compensation phase or entropy exceeds the established threshold, move on to Step 6; otherwise, it can be regarded that the final compensation phase θ_i is derived and proceed to Step 7.

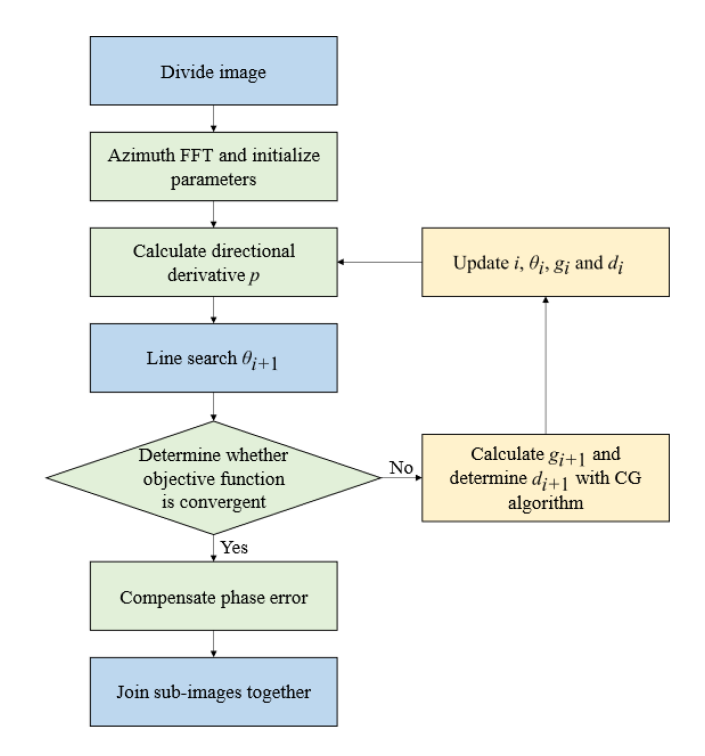


Fig. 7. Flowchart of the proposed algorithm.

Step 6: Calculate the new gradient g_{i+1} with (24) and determine the new directional d_{i+1} with (26). Then proceed to the Step 3.

Step 7: Compensate phase errors on the subimages accordingly and perform the azimuth IFFT; finally, merge all the subimages together in the time domain.

IV. EXPERIMENTS

In this section, validation of the proposed method is carried out using both simulation and real data.

A. Focusing Quality Evaluation Criteria and Methods for Comparison

Besides image entropy, image sharpness and image contrast are used as indicators to measure the focusing quality of images. The higher the focusing quality of an image, the greater its sharpness and contrast. First, the image entropy has been defined in (17). Root-mean-square contrast (RMSC) index is used to describe the contrast of an image and defined as [28]

$$RMSC(f) = \sqrt{\frac{1}{MN} \sum_{i=0}^{M-1} \sum_{j=0}^{N-1} (f^2(i,j) - \overline{f}^2(i,j))^2}.$$
(28)

The image sharpness *S* is defined as follows:

$$S(f) = -\sum_{m=0}^{M-1} \sum_{n=0}^{N-1} \ln(|f(m,n)|^2 + b).$$
 (29)

It has been proved that the maximum-posterior estimator is applied for estimating the phase error, where the parameter *b* in the equation can be construed as representing the background

TABLE IV PSEUDOCODE FOR THE CG METHOD

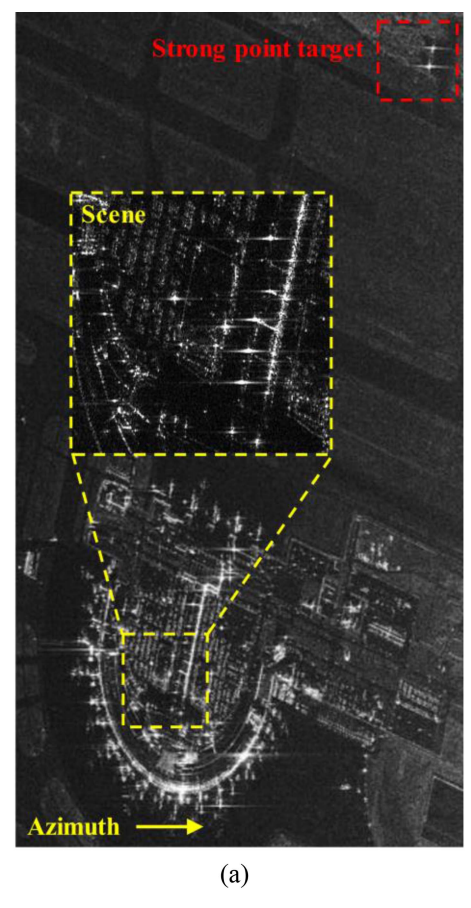
Algorithm2 Conjugate gradient method.

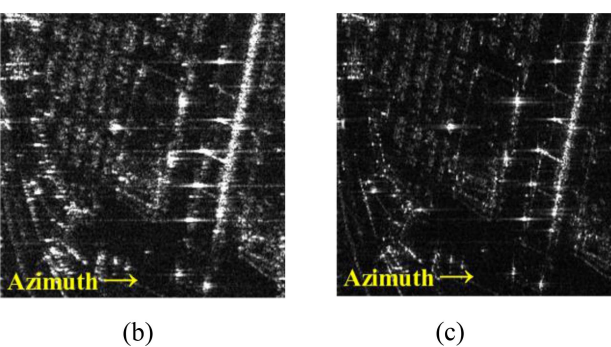
```
Input: SLC image I, division paremeter L, convergence thresholds
\Delta\theta th, \Delta E th.
Output: Phase-compensated image I_compensated.
1: // Step 1: Image division
2: SubImages \{I_l\}_{l=1,...,L} = divide_subimages (I, L);
3: for each I<sub>l</sub> in subImages do
4: // Step 2: Azimuth FFT and initialization
5: F = Azimuth IFFT (I_l);
6: // Initial compensation phase, search direction, step size and
iteration index
7: \theta_0 = 0, d_0 = 0, h_0 = 10^{-3}, i = 0;
8: E_0 = \text{compute entropy}(I_l);
                                                                 // (20)
9: // Iterative optimization loop
10: while True do
       // Step 3: Compute directional derivative
11:
12:
        g_i = compute gradient (F, \theta_i);
                                                                 // (24)
13:
        p = -d_i \cdot g_i; //Calculate the directional derivative, (27)
14:
       // Step 4: Line search update
       [\theta_{i+1}, h_{i+1}] = \text{line\_search} (F, \theta_i, d_i, h_i); //\text{Algorithm1 in TABLE}
15:
III and (25)
16:
        E_{i+1} = \text{compute\_entropy} (I_i \otimes \exp(-j\theta_{i+1}));
                                                                  // (20)
17:
       // Step 5: Convergence check
18:
        \Delta\theta = ||\theta_{i+1} - \theta_i||_2;
19:
        \Delta E = |E_{i+1} - E_i|;
        if \Delta \theta < \Delta \theta th or \Delta E < \Delta E th then
20:
21:
         break
22.
        end if
23:
       // Step 6: Update gradient and direction
24:
       g_{i+1} = \text{compute gradient } (F, \theta_{i+1});
                                                                   // (24)
25:
        d_{i+1} = \text{compute\_direction } (g_i, d_i);
                                                                   // (26)
26: end while
27: // Step 7: Compensation and reconstruction
28: F compensated = F \cdot \exp(-j\theta_{new});
29: I<sub>l</sub> compensated = Azimuth IFFT (F compensated);
30: end for
31: // Final image reconstruction
32: I\_compensated = join\_subimages (I_l\_compensated);
```

intensity [29]. For strong point targets, impulse response width (IRW), peak sidelobe ratio (PSLR), and integrated sidelobe ratio (ISLR) are utilized to evaluate the focusing quality. In simulation experiment, root-mean-square (rms) of the difference between the simulated and the estimated error serves as a measure to evaluate the accuracy of error estimation.

33: return I compensated.

To verify the effectiveness of the proposed method this article selects the PGA algorithm [16], the ADAM based on the minimum entropy criterion [19], and the BFGS method [18] for comparison. In the PGA algorithm, the window spacing is set to 15 dB below the peak point, the window shape is rectangular, and maximum likelihood estimation is used to estimate the phase error. The ADAM optimizer is configured with an initial learning rate of 0.1, an accumulation gradient exponential decay rate of 0.9, and an accumulation square gradient exponential decay rate of 0.999. Both the ADAM method and the BFGS method are based on the same entropy as the proposed method. In the proposed method, the initial line search step size is 10⁻³. For the restart strategy, Q in (26) is defined as 7.





TerraSAR-X data simulation experiment. (a) Original image. (b) Image with simulated error. (c) Compensated result with the proposed method.

B. Simulation Results

The simulated phase errors in a real TerraSAR-X image are firstly used to verify the proposed method, which evaluates the performance and the accuracy of the proposed method with an urban scene and strong point targets.

Fig. 8(a) shows a TerraSAR-X image of staring spotlight mode in Tsingtao, China, which includes an urban area with some buildings and several strong targets. The yellow zoomed patch presents detail of the experimental scene and the red box includes two strong point targets on the top of image. Fig. 8(b) shows the scene target with simulated phase errors in azimuth and the image is obviously defocused. Fig. 8(c) shows the scene target

TABLE V
COEFFICIENTS OF SIMULATED PHASE ERRORS

Error Coefficient	Value
Second order	17.0
Third order	-25.0
Fourth order	-15.0
Fifth order	12.0
Sixth order	-24.0
Random error	0.7

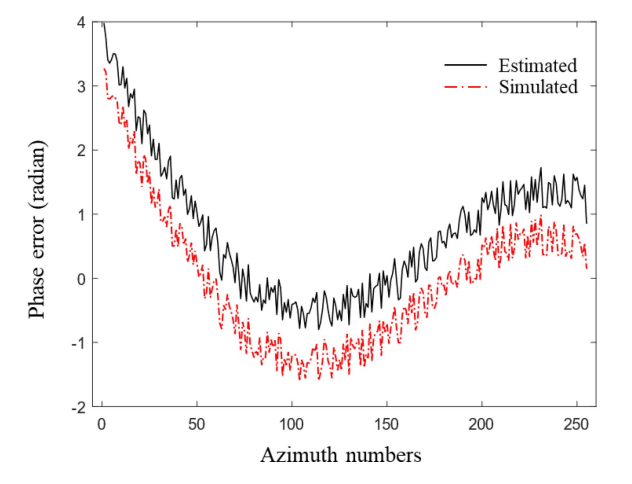


Fig. 9. Comparison of simulated phase error (in red) and estimated phase error (in black)

compensated with the proposed method, which is well focused. The simulated phase errors in Fig. 8 consist of second to sixth-order terms, as well as a random phase, according to the phase error model in (12). The simulation coefficients of phase errors are presented in Table V and the same coefficients are applied in both the scene target and the strong point target.

Fig. 9 shows curves of simulated and estimated phase for the proposed method applied in the urban area (yellow boxed area). The simulated (dotted red curve) and the estimated (solid black curve) phase errors have been offset vertically from each other for display purposes. The added higher order phase error as well as the random phase error are well estimated. The rms error between the traces is 0.062 rad.

Table VI displays the experimental results of simulating phase errors estimation. Two sets of experiments are conducted for the whole scene marked in yellow and the point target indicated in red. Four measured indices (entropy, sharpness, contrast, and rms) are used to evaluate the scene targets, while four measured indices (IRW, PSLR, ISLR, and rms) are used to evaluate the point targets. Among them, the rms of simulation image is the rms of simulation error itself, while the rest are the rms of the difference between simulation error and estimation error. In addition to the PGA algorithm, the other three optimization algorithms need to remove the linear term in the estimated phase through linear fitting, and then compare them with the simulated phase errors.

TABLE VI EVALUATION RESULT OF SIMULATED PHASE ERRORS

Index	Simulation	Proposed	PGA	ADAM	BFGS		
macx	image	method	method	method	method		
	Eval	uated indic	ators of sce	ene			
Entropy ↓	7.524	6.533	6.862	7.292	6.555		
Sharpness ↑	1.5440e6	1.5471e6	1.5455e6	1.5455e6	1.5471e6		
Contrast ↑	2.150	2.534	2.307	2.325	2.522		
RMS/rad \downarrow	2.13	0.062	0.251	0.980	0.093		
Evaluated indicators of strong point targets							
IRW/m ↓	0.579	0.385	0.385	0.342	0.386		
PSLR/dB↓	-2.83	-11.15	-12.35	-3.64	-10.06		
ISLR/dB↓	-2.30	-8.70	-8.14	-3.15	-8.57		
RMS/rad ↓	2.13	0.071	0.226	0.999	0.140		

Bold formatting highlights metrics where our method achieves better results compared to baseline methods.

Overall, all four methods have improved the focusing quality of the two types of targets. Among them, the ADAM method performs slightly worse than the other three. The PGA method performs well, especially in strong point target scenes. The BFGS method and the proposed method perform better than the other two and their metrics are relatively close. For specific metrics, the proposed method's PSLR is worse than the PGA method, and although the ADAM method's IRW is better, its point target is not focused. In all other remaining metrics, the proposed method has the best performance.

C. Real Data Experimental Results

The real data experiments include the commercial satellites Pujiang-II and UMBRA-01, various modes, and targets of different sizes and types, to assess the efficacy of the proposed method using real spaceborne SAR data across different application scenarios.

Image A and Image B represent urban areas in Wuhan, China, captured under the slide spotlight mode of the Pujiang-II satellite, with Image A being a slice of one of the buildings in Image B. Image C shows a high-rise building from Fig. 5, captured by the UMBRA-01 satellite, with a resolution of 0.5 m. Fig. 10(a)–(f) presents the original images and the results after phase compensation for these three images.

In table VII, three indices (entropies, contrast, and sharpness values) of both the original images and refocused results are listed. In addition to the PGA algorithm, the other three iterative algorithms share the same stopping criterion, which is that the two-norm of the phase error calculated in two consecutive iterations is less than 0.001. All four algorithms improve the focusing quality of the original images for targets of different types and sizes, with the BFGS algorithm and the proposed method demonstrating significantly superior performance compared to the other two approaches. Notably, the proposed one outperforms all other methods across all metrics.

The following is a comparative experiment between block processing and overall processing of the high-rise building in Image C. Fig. 11(a), (c), and (e) demonstrates that there is a

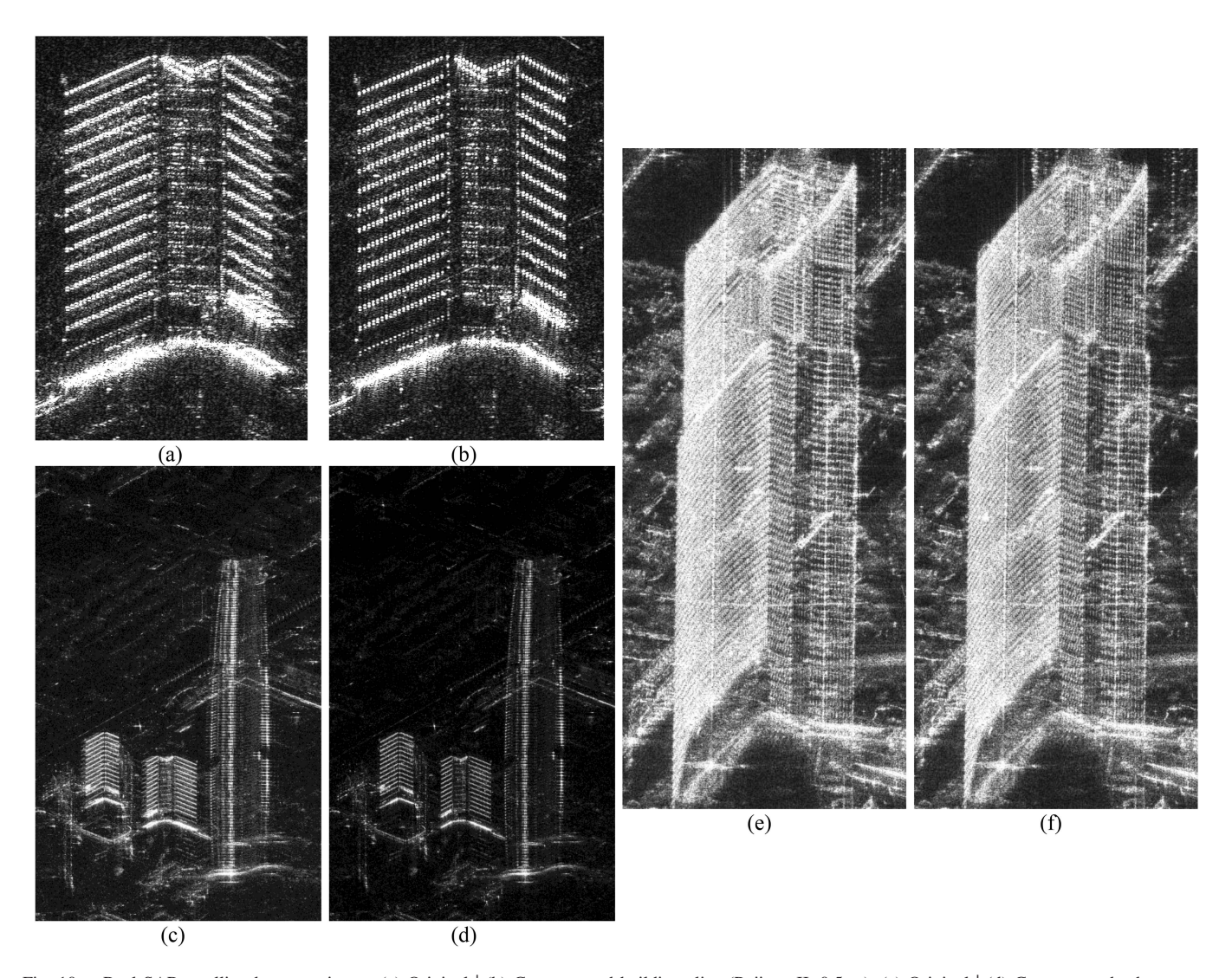


Fig. 10. Real SAR satellite data experiment. (a) Original | (b) Compensated building slice (Pujiang-II, 0.5 m). (c) Original | (d) Compensated urban scene (Pujiang-II, 0.5 m). (e) Original | (f) Compensated Keangnam Tower (UMBRA-01, 0.5 m).

TABLE VII
EVALUATION RESULT OF REAL SPACEBORNE DATA

	Measured indices for different targets of different sizes (azimuth×range)								
Method	Image A,	, Building	1(600×390)	Image B,	Building 2(3000×1700)	Image C, l	Building 3	(550×1200)
	E↓	C↑	S↑	E↓	C↑	S↑	E↓	C↑	S↑
Original	9.046	2.242	-3.6964e5	16.522	2.281	84.064	11.398	1.660	-4.7450e6
PGA	8.957	2.284	-3.6798e5	16.439	2.301	85.586	11.338	1.683	-4.7398e6
Adam	8.873	2.299	-3.6698e5	16.433	2.300	85.599	11.337	1.683	-4.7398e6
BFGS	8.652	2.508	-3.6144e5	16.170	2.374	91.234	11.331	1.686	-4.7391e6
Proposed	8.646	2.512	-3.6138e5	16.167	2.375	91.271	11.256	1.706	-4.7312e6

Bold formatting highlights metrics where our method achieves better results compared to baseline methods.

significant difference in the degree of focus at different heights of the building in the original image, with the bottom being well-focused and the top noticeably defocused. If phase error estimation is directly performed on this image, the process will be dominated by the building top. As a result, the overall focusing quality, especially at the top, may improve, but the

focusing quality at the bottom may deteriorate. Therefore, it is necessary to perform block processing on this image.

The image is divided into three blocks (top, middle, and bottom) along its range direction, and phase error estimation and compensation are then performed for each subimage separately. Fig. 11(b), (d), and (f) shows the subimages after phase error

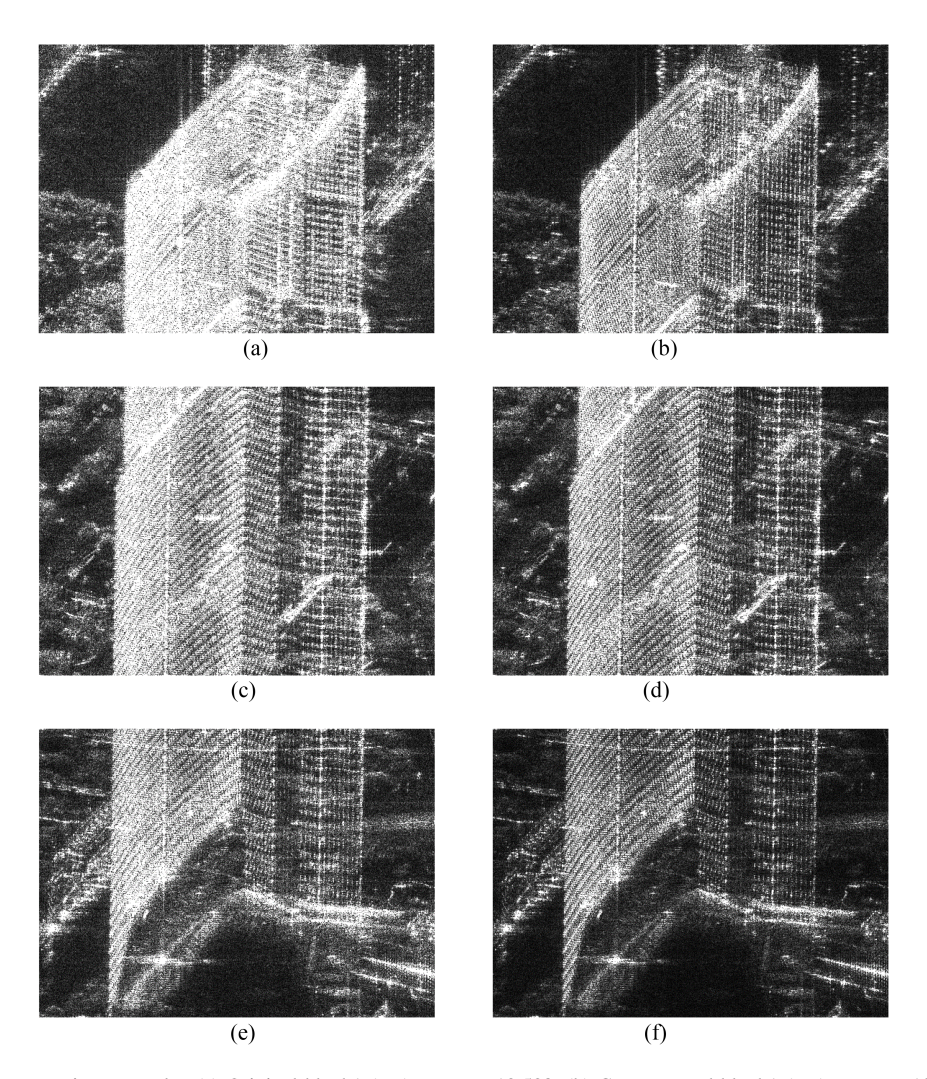


Fig. 11. Block processing experiment results. (a) Original block1 (top), entropy 10.508. (b) Compensated block1 (top), entropy 10.194. (c) Original block2 (middle), entropy 10.454. (d) Compensated block2 (middle), entropy 10.313. (e) Original block3 (bottom), entropy 10.007. (f) Compensated block3 (bottom), entropy 9.999.

compensation, with the most significant quality improvement observed in the image of the building's top (Block 1). Fig. 12 presents the estimated phase errors, where the black solid line, red dash-dotted line, and blue dashed line represent the phase curves for the top, middle, and bottom of the building, respectively. The three curves exhibit similar trends, but the black phase error curve of the building top exceeds $\pi/4$, which causes noticeable defocusing, while the phase error curve of the building bottom is very small and will not lead to defocusing. The red curve falls between the two.

Table VIII provides detailed measured indices, further validating the above-mentioned observation. Evaluation of the entire image includes the original image, the results without block processing, and the results from block processing. Results show that our method has significantly enhanced image quality. Analyzing the subimages reveals a progressive enhancement in focusing quality from top to bottom. Taking image entropy as an example, the top section is improved by 3%, the middle section by 1.8%, and the bottom section by 0.8%.

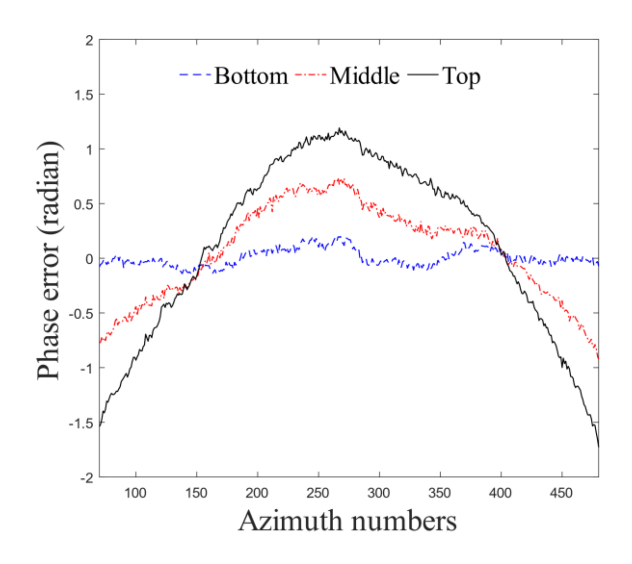


Fig. 12. Comparison of phase errors at different heights of Keangnam Landmark Tower 72, Hanoi, Vietnam.

TABLE VIII
EVALUATION RESULT OF SUB-IMAGES

Images		Measured indices			
		Entropy↓	Contrast↑	Sharpness↑	
	Original	11.398	1.660	-4.745e6	
Whole image	Global comp.	11.330	1.683	-4.739e6	
	Block comp.	11.256	1.706	-4.731e6	
Dlaglet (tom)	Original	10.508	1.628	-1.545e6	
Block1 (top)	Compensated	10.194	1.724	-1.522e6	
Block2	Original	10.454	1.613	-1.593e6	
(middle)	Compensated	10.313	1.655	-1.590e6	
Block3	Original	10.007	1.732	-1.597e6	
(bottom)	Compensated	9.999	1.736	-1.596e6	

TABLE IX
COMPUTATIONAL COMPLEXITY ANALYSIS

Processing step	Complexity (FLOP)			
	Sub function Sub function			
Image compensation	$2MN^2+5N^2+MN+3N$			
Entropy calculation	$2MN^2 + 5N^2 + 7MN + 5N$			
Gradient calculation	$2MN^2 + 5N^2 + 10MN + 7N$			
Wolfe line search	$4Grad-6MN+5N+F_1(6Grad-12MN+6N)$			
Interpolation method	$2Grad+12N+F_1(2Grad-6MN-2N)$			
Comparison	of phase compensation method			
PGA	48MN+24N+12M			
Adam	$6MN+F_2(2MN^2+5N^2+10MN+20N)$			
BFGS	$6MN+F_2(2N^3+2MN^2+22N^2+23N+Wolfe)$			
Proposed	$6MN+F_2(2MN^2+5N^2+10MN+11N+Interp.)$			

Bold formatting highlights metrics where our method achieves better results compared to baseline methods.

D. Algorithm Efficiency Analysis

To evaluate the efficiency of algorithms, their computational complexity is an important metric. In the following, we calculate the complexity based on the number of floating-point operations (FLOP) of four methods from the aforementioned experiments. The results of this analysis are presented in Table IX, where M represents image range size, N denotes image azimuth size, and Grad indicates the FLOP for performing a single gradient calculation. F_1 and F_2 represent the number of iterations for 1-D line search and the total number of iterations for the algorithm, respectively. In the BFGS method and the proposed method, 1-D line search methods based on the Wolfe criterion and the interpolation-based line search are respectively applied. Constant terms are ignored in the table.

It shows that the complexity increases with the increase of F_1 and F_2 , as well as the image size M and N. The PGA method performs only 6 fixed iterations without the need for gradient calculation, resulting in the lowest complexity. The remaining three methods require more iterations, with the Adam method often having much more. However, it does not require line search, and overall, its complexity is lower than the other two methods. Compared to the BFGS quasi-Newton method, the proposed one clearly has a lower complexity. And the complexity of the proposed interpolation-based line search method is also lower than the line search based on the Wolfe criterion.

Taking the building of image D as an example, Fig. 13 compares the image entropy curves of these four methods, where no block dividing processing is involved. The proposed method,

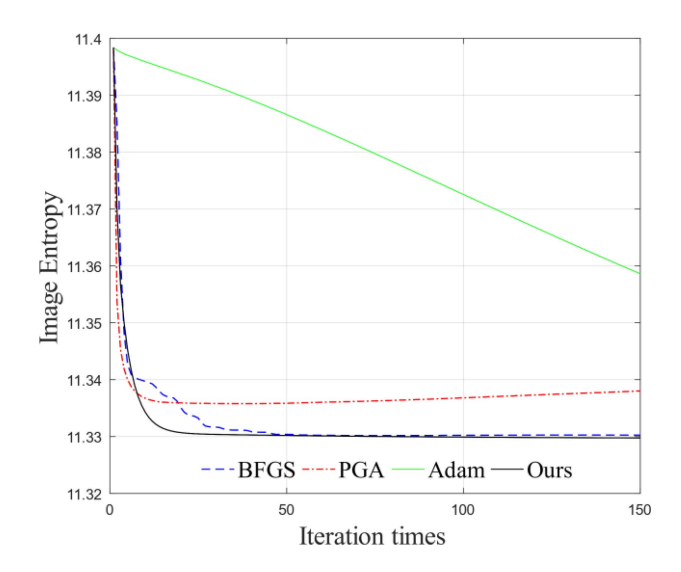


Fig. 13. Image entropy versus iteration times of the four methods.

TABLE X ALGORITHM RUNNING TIME COMPARISON

		Processir	ng time(s)	
Algorithms	Image A	Image B	Image C	Image D
PGA	0.64	0.69	8.69	2.94
Adam	9.06	14.10	145.64	22.19
BFGS	20.55	23.68	449.13	13.94
Proposed	17.85	20.71	254.55	6.34

Bold formatting highlights metrics where our method achieves better results compared to baseline methods.

along with the BFGS algorithm, achieves the best optimization results, and it converges with fewer iterations and ultimately attains a slightly better image entropy than the BFGS method. Compared to the other three methods, the PGA algorithm can rapidly approach a smaller image entropy with just a few iterations but it lacks in terms of convergence, leading to an unsatisfactory final optimization result. The Adam algorithm, as it does not require line search, also has a fast speed per iteration, but its final optimization effect is worse than that of the other three. Overall, our proposed method has a clear advantage in terms of both processing effectiveness and efficiency, which is also confirmed by the results in Table X.

V. DISCUSSION

This study addressed defocusing in high-resolution SAR images of high-rise targets, primarily caused by spatially variant QPE induced by height. The proposed method combines block processing with an FR-CG optimizer using minimum image entropy. Key contributions include effectively handling spatial variance through range-direction blocking and demonstrating superior focusing performance, outperforming methods, such as PGA, ADAM, and BFGS, on simulated and real data (Pujiang-II, UMBRA-01), while achieving superior computational efficiency versus BFGS.

Although validated on static urban structures, the method demonstrates broader applicability potential. For instance, azimuth phase errors in moving ships share a structural similarity with (12) and exhibit comparable spatial variance [19]. Consequently, future research should delineate its applicability boundaries and develop unified models and methods for broader scenarios, extending its utility.

While more efficient than BFGS, iterative optimization for large scenes remains computationally intensive, necessitating further acceleration for real-time applications. If sufficient diverse, high-quality training data becomes available, future work should explore deep learning models to directly estimate complex, spatially variant phase errors from defocused images, enabling faster inference. This is particularly relevant for datasets covering varied targets (buildings, ships), motions, and atmospheric conditions

VI. CONCLUSION

In high-resolution mode, phase errors occur in SAR images of tall buildings, and these phase errors vary with the height of the buildings, which makes SAR images become defocused. Through analysis and simulation, the phase error caused by target height is predominantly determined by the quadratic term. However, the quadratic coefficient exhibits spatial variation across range cells. Based on the analysis, a phase error model and a corresponding SLC SAR image model that includes phase errors are established. To compensate for the phase errors, an optimization algorithm based on the FR-CG method is introduced to estimate the phase error. To facilitate block processing and address the spatial variation issue of phase error, image entropy is adopted as the objective function. To improve processing efficiency, a momentum-based interpolation method is employed in the 1-D line search to determine the optimal step, and a restart strategy is adopted in the CG method. As demonstrated by experimental results, the proposed method achieves up to 4% improvement in image entropy for defocused images, outperforming other comparative algorithms. In terms of computational efficiency, it demonstrates nearly twofold enhancement over the BFGS algorithm under specific operational scenarios.

ACKNOWLEDGMENT

The authors would like to thank the Umbra Lab of California, USA, for providing the UMBRA-01 spaceborne SAR data.

REFERENCES

- [1] S. Montazeri, X. X. Zhu, M. Einder, and R. Bamler, "Three-dimensional deformation monitoring of urban infrastructure by tomographic SAR using multitrack TerraSAR-X data stacks," *IEEE Trans. Geosci. Remote Sens.*, vol. 54, no. 12, pp. 6868–6878, Dec. 2016.
- [2] F. Lombardini, F. Cai, and D. Pasculli, "Spaceborne 3-D SAR tomography for analyzing garbled urban scenarios: Single-look superresolution advances and experiments," *IEEE J. Sel. Topics Appl. Earth Observ. Remote Sens.*, vol. 6, no. 2, pp. 960–968, Apr. 2013.
- [3] Y. Guan, H. Xu, W. Liu, C. Li, and Y. Liu, "A false-alarm-controllable modified AdaBoost wake detection method using SAR images," *IEEE Sensors J.*, vol. 23, no. 23, pp. 29394–29405, Dec. 2023.

- [4] C. N. Koyama and M. Sato, "Detection and classification of subsurface objects by polarimetric radar imaging," in *Proc. IEEE Radar Conf.*, 2015, pp. 440–445.
- [5] L. Li, C. Wang, H. Zhang, and B. Zhang, "Residual Unet for urban building change detection with Sentinel-1 SAR data," in *Proc. IGARSS* 2019 - 2019 IEEE Int. Geosci. Remote Sens. Symp., 2019, pp. 1498–1501.
- [6] Y. K. Deng, W. D. Yu, H. Zhang, W. Wang, D. C. Liu, and R. Wang, "Forthcoming spaceborne SAR development," *J. Radars*, vol. 9, no. 1, pp. 1–33, 2020.
- [7] W. L. Du, Y. Zhou, J. Zhao, and X. Tian, "K-means clustering guided generative adversarial networks for SAR-optical image matching," *IEEE Access*, vol. 8, pp. 217554–217572, 2020.
- [8] F. Amjadipour, H. Ghassemian, and M. Imani, "Building detection using very high resolution SAR images with multi-direction based on weightedmorphological indexes," in *Proc. 2022 Int. Conf. Mach. Vis. Image Pro*cess., 2022, pp. 1–6.
- [9] S. Saha, F. Bovolo, and L. Bruzzone, "Building change detection in VHR SAR images via unsupervised deep transcoding," *IEEE Trans. Geosci. Remote Sens.*, vol. 59, no. 3, pp. 1917–1929, Mar. 2021.
- [10] T. M. Calloway and G. W. Donohoe, "Subaperture autofocus for synthetic aperture radar," *IEEE Trans. Aerosp. Electron. Syst.*, vol. 30, no. 2, pp. 617–621, Apr. 1994.
- [11] J. Li, J. Chen, W. Liu, P. Wang, and C. Li, "A synthetic bandwidth method for high-resolution SAR based on PGA in the range dimension," *Sensors*, vol. 15, no. 7, pp. 15339–15362, 2015.
- [12] L. Yang, M. Xing, Y. Wang, L. Zhang, and Z. Bao, "Compensation for the NsRCM and phase error after polar format resampling for airborne spotlight SAR raw data of high resolution," *IEEE Geosci. Remote Sens. Lett.*, vol. 10, no. 1, pp. 165–169, Jan. 2013.
- [13] J. Huo, M. Li, Z. Li, J. Wu, and J. Yang, "Novel SAR autofocus method based on Deep learning with GAN network," in *Proc. 2021 CIE Int. Conf. Radar*, 2021, pp. 800–803.
- [14] L. Hu, J. Wei, S. Su, S. Huang, Z. Zhao, and X. Tong, "A new SAR autofocus method based on error coefficient optimization," in *Proc.* 2024 10th Int. Conf. Comput. Commun., 2024, pp. 746–750.
- [15] T. Zhang, Y. Li, T. Zhang, and T. Gu, "Expediting phase gradient autofocus algorithm for SAR imaging," in *Proc. IGARSS IEEE Int. Geosci. Remote Sens. Symp.*, 2020, pp. 1145–1148.
- [16] A. S. El-tanany, K. Hussein, A. Mousa, and A. S. Amein, "Evaluation of gradient descent optimization method for SAR images Co-registration," in *Proc.* 2020 12th Int. Conf. Elect. Eng., 2020, pp. 288–292.
- [17] J. Wang, T. Lai, Q. Wang, H. Huang, and X. Wang, "Entropy-based parameterized amplitude and phase correction for MIMO groundbased SAR," *IEEE Trans. Geosci. Remote Sens.*, vol. 62, 2024, Art. no. 5215014.
- [18] J. Chen, K. Wang, and W. Yang, "Accurate estimation of stitching error for high-resolution multi-sub-bands SAR system with image sharpness analysis," *Electron. Lett.*, vol. 52, pp. 1948–1950, 2016.
- [19] Z. Y. Li, J. Y. Guo, Y. T. Zhang, L. J. Huang, J. Li, and Y. R. Wu, "A novel autofocus algorithm of ship target in SAR image based on the adaptive momentum estimation optimizer and space-variant minimum entropy criteria," *J. Radars*, vol. 11, no. 1, pp. 83–94, 2022.
- [20] C. T. Kelley and E. W. Sachs, "Quasi Newton methods and unconstrained optimal control problems," in *Proc. 1986 25th IEEE Conf. Decis. Control*, 1986, pp. 1829–1831.
- [21] I. G. Cumming and F. H. Wong, "Digital signal processing of synthetic aperture radar data: Algorithms and implementation," Norwood, MA: Artech House, 2005.
- [22] X. L. Huang, K. F. Ji, X. G. Leng, G. G. Dong, and X. W. Xing, "Refocusing moving ship targets in SAR images based on fast minimum entropy phase compensation," *Sensors*, vol. 19, no. 5, 2019, Art. no. 1154.
- [23] R. L. Morrison, M. N. Do, and D. C. Munson, "SAR image autofocus by sharpness optimization: A theoretical study," *IEEE Trans. Image Process.*, vol. 16, no. 9, pp. 2309–2321, Sep. 2007.
- [24] M. L. Qiao, M. Xu, L. Jiang, P. Kei, S. J. Wen, and Y. J. Chen, "HyperSOR: Context-aware graph hypernetwork for salient object ranking," *IEEE Trans. Pattern Anal. Mach. Intell.*, vol. 46, no. 9, pp. 5873–5889, Sep. 2024.
- [25] D. Kasilingam, J. F. Wang, J.-S. Lee, and R. Jensen, "Focusing of synthetic aperture radar images of moving targets using minimum entropy adaptive filters," in *Proc. IGARSS IEEE 2000 Int. Geosci. Remote Sens. Symp. Taking Pulse Planet: Role Remote Sens. Manag. Environ. Proc.*, 2000, vol. 1, pp. 74–76.

- [26] T. Xiong, M. Xing, Y. Wang, S. Wang, J. Sheng, and L. Guo, "Minimum-entropy-based autofocus algorithm for SAR data using Chebyshev approximation and method of series reversion, and its implementation in a data processor," *IEEE Trans. Geosci. Remote Sens.*, vol. 52, no. 3, pp. 1719–1728, Mar. 2014.
- [27] F. Liu, H. Wang, and H. Hao, "Fletcher-reeves conjugate gradient for sparse reconstruction: Application to image compressed sensing," in *Proc.* 2009 2nd Asian-Pacific Conf. Synthetic Aperture Radar, 2009, pp. 322–325.
- [28] L. Xi, G. S. Liu, and J. J. Ni, "Autofocusing of ISAR images based on entropy minimization," *IEEE Trans. Aerosp. Electron. Syst.*, vol. 35, no. 4, pp. 1240–1252, Oct. 1999.
- [29] T.J. Schulz, "Optimal sharpness function for SAR autofocus," *IEEE Signal Process. Lett.*, vol. 14, no. 1, pp. 27–30, Jan. 2007.



YaMin Wang received the M.S. and Ph.D. degrees in information and communication engineering from Beihang University [previously known as Beijing University of Aeronautics and Astronautics (BUAA)], Beijing, China, in 2016 and 2022, respectively

From 2022 to 2024, she was a Postdoctoral with the School of Electronics and Information Engineering, BUAA, where she has been an Assistant Professor since 2024. Her research interests include synthetic aperture radar (SAR), video SAR, ground moving

target indication, and SAR signal processing.



JiaDong Deng was born in 1995. He received the B.S. degree in information and computational science from Beihang University, Beijing, China, in 2017, where he is currently working toward the Ph.D. degree in signal and information processing.

His research interests include spaceborne synthetic aperture radar image formation for terrain observation by progressive scans mode and sliding spotlight mode.



Jiayi Guo was born in 1996. She received the B.S. and Ph.D. degrees in signal and information processing from Beihang University, Beijing, China, in 2018 and 2024. respectively.

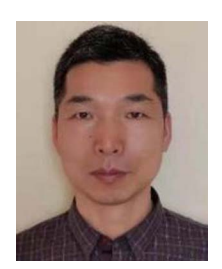
Since 2024, she has been a Postdoctoral Researcher with the School of Information and Communication Engineering, Communication University of China, Beijing, China. Her research interests include SAR image formation and SAR image quality improvement.



Wei Yang (Member, IEEE) was born in 1983. He received the M.S. and Ph.D. degrees in signal and information processing from Beihang University (BUAA), Beijing, China, in 2008 and 2011, respectively.

From 2011 to 2013, he was a Postdoctoral with the School of Electronics and Information Engineering, BUAA, where he has been a Lecturer with the School of Electronics and Information Engineering, since 2013. From 2016 to 2017, he was a Visiting Researcher with the Department of Electronic and Electrical Engineering, The University of Sheffield,

Sheffield, U.K. Since 2018, he has been an Associate Professor with the School of Electronics and Information Engineering, BUAA, and a Professor since 2023. He has authored or coauthored more than 60 journals and conference publications. His research interests include moving target detection, high-resolution spaceborne synthetic aperture radar (SAR) image formation, SAR image quality improvement, and 3-D imaging.



Wei Xiong received the B.S. degree in radar engineering, and the M.S. and Ph.D. degrees in information and communication engineering from Naval Aviation University, Yantai, China, in 1998, 2001, and 2005, respectively.

From 2007 to 2009, he was a Postdoctoral Researcher with the Department of Electronic Information Engineering, Tsinghua University, Beijing, China. He is currently a Full Professor with Naval Aviation University, where he teaches random signal processing and information fusion. He is one of the

Founders and the Directors of the Institute of Information Fusion, Naval Aviation University. His research interests include pattern recognition, remote sensing, and multisensor information fusion.

Dr. Xiong is a Member and the Director General of the Information Fusion Branch of the Chinese Society of Aeronautics and Astronautics.



HongCheng Zeng (Member, IEEE) was born in 1989. He received the Ph.D. degree in signal and information processing from Beihang University, Beijing, China, in 2016.

From 2016 to 2019, he was a Postdoctoral with the School of Electronics and Information Engineering, Beihang University, where he has been an Assistant Professor since August 2019. From 2017 to 2018, he was a Visiting Researcher with the School of Mathematics and Statistics, The University of Sheffield, Sheffield, U.K. Since 2022, he has been an Associate

Professor with the School of Electronics and Information Engineering, Beihang University. He has authored or coauthored more than 30 journal and conference publications. His research interests include high-resolution spaceborne SAR image formation, passive radar signal processing, and moving target detection.



sounding

Min Liu was born in Chongqing, China, in 1986. She received the Ph.D. degree in communication and information systems from Beihang University, Beijing, China, in 2014.

Since 2018, she has been a Senior Engineer with the Qian Xuesen Laboratory of Space Technology, China Academy of Space Technology, Beijing, China. Her research interests include synthetic aperture radar (SAR) image processing, SAR image quality improvement, SAR image geolocation without ground control points, and tomographic imaging for radar



Jie Chen (Senior Member, IEEE) was born in 1973. He received the B.S. and Ph.D. degrees in information and communication engineering from Beihang University, Beijing, China, in 1996 and 2002, respectively.

Since 2004, he has been an Associate Professor with the School of Electronics and Information Engineering, Beihang University. From 2009 to 2010, he was a Visiting Researcher with the School of Mathematics and Statistics, The University of Sheffield, Sheffield, U.K., working on ionospheric effects on

low-frequency space radars that measure forest biomass and ionospheric electron densities. Since July 2011, he has been a Professor with the School of Electronics and Information Engineering, Beihang University. His research interests include multimodal remote sensing data fusion, topside ionosphere exploration with spaceborne HF/VHF-synthetic aperture radar (SAR) systems, high-resolution spaceborne SAR image formation, and SAR image quality enhancement.



Wei Liu (Senior Member, IEEE) received the B.Sc. degree in space physics and the L.L.B. degree in intellectual property law from Peking University, Beijing, China, in 1996 and 1997, respectively, the M.Phil. degree from the Department of Electrical and Electronic Engineering, University of Hong Kong, Hong Kong, in 2001, and the Ph.D. degree from the School of Electronics and Computer Science, University of Southampton, Southampton, U.K., in 2003.

He was a Postdoc first at Southampton and later with Imperial College London, London, U.K. From

2005 to 2023, he was a Lecturer/Senior Lecturer with the Department of Electronic and Electrical Engineering, University of Sheffield, Sheffield, U.K., and from 2023 to 2024, a Reader with the School of Electronic Engineering and Computer Science, Queen Mary University of London. Since 2024, he has been a Professor with the Department of Electrical and Electronic Engineering, Hong Kong Polytechnic University, Hong Kong. He is currently a Visiting Professor. He has authored or coauthored more than 480 journal and conference papers, six book chapters, and two research monographs titled "Wideband Beamforming: Concepts and Techniques" (Wiley, 2010) and "Low-Cost Smart Antennas" (Wiley, 2019), respectively. His research interests include sensor array and multichannel signal processing and its various applications, such as robotics and autonomous systems, human—computer interface, radar, sonar, and wireless communications.

Dr. Liu is a Member of the Applied Signal Processing Systems Technical Committee (Vice-Chair for 2025–2026) of the IEEE Signal Processing Society (SPS), the Digital Signal Processing Technical Committee (Chair for 2022-2024) of the IEEE Circuits and Systems Society, and the IEEE SPS Education Board (2024–2026, Chair of its Educational Conference Program Committee), and a former member of the Sensor Array and Multichannel Signal Processing Technical Committee of the IEEE SPS (Chair for 2021-2022), the IEEE SPS Technical Directions Board (2021-2022), and the IEEE SPS Conference Board and its Executive Subcommittee (2022-2023). He also acted as an Associate Editor for IEEE TRANSACTIONS ON SIGNAL PROCESSING, IEEE ACCESS, and Journal of the Franklin Institute, and an Executive Associate Editor-in-Chief for the Journal Frontiers of Information Technology and Electronic Engineering. He is currently an Associate Editor for the IEEE TRANSACTIONS ON CIRCUITS AND SYSTEMS I: REGULAR PAPERS and IEEE ANTENNAS AND WIRELESS PROP-AGATION LETTERS. He is an IEEE Distinguished Lecturer for the Aerospace and Electronic Systems Society (2023–2026).